Progress In Electromagnetics Research, PIER 40, 177–205, 2003

POTENTIAL OF REFLECTED GNSS SIGNALS FOR ICE SHEET REMOTE SENSING

M. Wiehl

Technische Universität Dresden
Institut für Planetare Geodäsie
01062 Dresden, Germany

B. Legrésy

Laboratoire d' Etudes en Géophysique et Océanographie Spatiales (LEGOS)
18 Av. E. Belin, 31401 Toulouse Cedex 4, France

R. Dietrich

Technische Universität Dresden
Institut für Planetare Geodäsie
01062 Dresden, Germany

Abstract—Earth-reflected GNSS (Global Navigation Satellite System) signals have become an attractive tool for remote sensing, e.g., ocean altimetry and scatterometric ocean wind measurements. For ice sheets, the large penetration capability and the large-scale surface averaging of the L-band signals could open a new look on firnpack characteristics like accumulation rates. In this paper we investigate theoretically reflections of GPS (Global Positioning System) signals from ice sheets. We derive a model of the reflection signal and perform simulations of airborne and spaceborne measurements. The results show that the signal, though complex, is sensitive to the roughness of the snow surface (and internal interfaces) and to firn parameters like accumulation rates. To extract valuable and concise information from the complex signal, we derive an example procedure that focusses on particular ground zones during a satellite receiver pass. The results indicate that it should be possible in principle to separately infer surface and firnpack parameters from the measurements. We conclude that GNSS reflections over ice sheets should be further persued, in particular by obtaining experimental data.

1 Introduction

2 A Model for GPS Ice Reflection
- 2.1 Basic Concepts
  - 2.1.1 Signal and Receiver Structure
  - 2.1.2 Radar Equation for GPS Surface Reflections
  - 2.1.3 Reflection Geometry, Range and Doppler Zones
- 2.2 Ice Surface Reflection
- 2.3 Subsurface Reflection
  - 2.3.1 Internal Layering as the Reflection Source
  - 2.3.2 Directivity Assumption and Uniformity Approximations
  - 2.3.3 Analytical Model Derivation
- 2.4 Evaluation of Model Parameters
  - 2.4.1 Surface Scattering
  - 2.4.2 Subsurface Scattering
  - 2.4.3 Signal Path through Firn

3 Numerical Simulations
- 3.1 General Approach
- 3.2 Simulation Description

4 Results
- 4.1 Simulated Measurement Scenarios
- 4.2 Qualitative Studies with Idealised Interfaces
  - 4.2.1 Waveform Shape
  - 4.2.2 Effect of Subsurface Contribution
  - 4.2.3 Effect of Roughness
- 4.3 Account for Topographic and Roughness Variations
- 4.4 Focussing on Subzones
  - 4.4.1 Concept of Focussing on Subzones During a Satellite Pass
  - 4.4.2 Focussing Procedures

5 Conclusions

Acknowledgment

References

1. INTRODUCTION

Earth-reflected GNSS (Global Navigation Satellite System) signals can be used for remote sensing. This prospect has attracted growing research interest in the last years. Since GNSS signals are provided free of charge, only passive instruments are needed. Since one receiver can simultaneously receive signals from several satellites, a high resolution in space and time can be obtained. In addition to GPS (Global Positioning System), the Russian GLONASS (Global Navigation Satellite System) and the future European GALILEO system will further expand the application potential. The geometry of bistatic radar, i.e., with different transmitter and receiver positions, leads to generally non-vertical forward reflections and thus offers remote sensing potentials complementary to those of vertical incidence and backward scattering.

The concept of using reflected GPS signals for ocean observations was proposed in 1993 by Martin-Neira [1]. First airborne and spaceborne detections of ocean-reflected GPS signals were reported by Auber et al. [2] and Lowe et al. [3]. Specialised receiver architectures and processing algorithms have been designed to appropriately map the reflection signal with respect to time delay and frequency [1, 4]. Altimetric applications over water have proved feasible in groundborne experiments [5, 6] and airplane campaigns [7]. In addition to the GPS navigation code, the use of the carrier phase information for altimetry has been investigated [8]. In a scatterometric approach, GPS reflections have been used to infer sea roughness parameters and thus wind speeds [9]. Ionospheric sensing [10], soil moisture measurements [11], and sea ice observations [12] are some other applications under investigation. Growing experience from space experiments is expected for the coming years. The german satellite missions CHAMP and the argentine-US mission SAC-C (both launched in 2000) carry nadir-looking GPS antennas for GPS reflection experiments. GPS occultation measurements from CHAMP contain earth-reflected signals with particularly high intensity over Antarctica [13]. Further space experiments are being planned.

Remote sensing of ice sheets shall essentially contribute to our understanding of the geosphere by describing the snow surface (e.g., its roughness) and the snowpack internal structures (e.g., related to snow accumulation). In particular, accumulation rates are poorly known over Antarctica so that recent data compilations like Vaughan et al. [14] are still very restricted by the poor coverage of in-situ measurements. Space techniques are the only possibility to overcome this problem. In this effort, numerous studies have involved microwave measurements

from radiometers, altimeters, scatterometters and SAR. Recently, Winnebrenner et al. [15] and Drinkwater et al. [16] established relations between accumulation rate and passive and active centimeter microwave measurements, respectively. However the accumulation rates obtained are averaged over depth and are therefore related to different time scales depending on the signal's penetration depth. The typical 5 to 10 meters penetration depth of Ku- and C-band signals corresponds to the last century accumulation regime, and SSMI-like infrared surveys correspond to present accumulation. Finally, the typically 100 meter penetration depth of L-band GNSS signals would relate to the millenium scale accumulation rate.

Applications of GNSS reflections may therefore open new perspectives for ice sheet remote sensing. The bistatic surface echoes may not allow accurate surface height measurements because the horizontal and range resolution are poor compared to radar and laser altimetry, and because L-band waves penetrate deep into the firn (see e.g., Rignot et al. [17]). However, the large-scale averaging of roughness and the strong penetrating capabilities may allow a new look on snowpack structures.

In this paper we concentrate on ice applications of GNSS reflections. In lack of experimental data we discuss theoretically the character of signal that can be foreseen. We derive a model of GPS signal reflection including surface and volume echoes (Section 2). We explain the simulation tools we have developed (Section 3) and present simulation results for airborne and spaceborne measurements (Section 4). The results show the signal's sensitivities to major parameters of both the Snow surface (together with internal interfaces) and the firnpack. They also show the high complexity of the reflection signal. To investigate how we can extract valuable and concise information from this complex signal, we derive an example procedure that focusses on particular ground zones during a satellite receiver pass (Section 4.4). By the results of this procedure we also indicate that it should be principally possible to separately infer surface and firnpack parameters from the measurements.

2. A MODEL FOR GPS ICE REFLECTION

2.1. Basic Concepts

2.1.1. Signal and Receiver Structure

For the complex structure of the GPS signal we shortly recall [18, 19] that it consists of two L-band carriers (L1 with 1.58 GHz and L2 with 1.23 GHz) with two pseudo-random noise (PRN) codes superimposed

by a binary biphase modulation. Their "chip length" τ_c (i.e., the time of constant state of the modulation function) corresponds to a range of 300 m for the C/A Code and 30 m for the P-Code.

We assume the way of recording reflected GPS signals described by Garrison et al. [4]: The reflected signal incident at the receiver is correlated with a reference signal shifted in time by τ and shifted in frequency by f_C to account for range delays and Doppler shifts. Squaring and incoherently averaging the correlator output yields the average receiver output power with respect to time delay and frequency shift. This function is called the "delay-Doppler waveform".

2.1.2. Radar Equation for GPS Surface Reflections

For surface reflections from ocean, Zavorotny and Voronovich [20] show that the average receiver output power W_s with respect to τ and f_C (i.e., the delay-Doppler waveform) can be expressed by an integral over the reflecting surface,

$$W_s(\tau, f_C) = \frac{T_i^2}{4\pi} \int_{\vec{x} \in \text{Surface}} D^2 \Lambda^2 |S|^2 R_t^{-2} R_r^{-2} \sigma_s^0 dA(\vec{x}). \tag{1}$$

Here, T_i is the coherent integration time for the correlation, $D^2 = D^2(\vec{x})$ is the receiver antenna gain. The triangular Λ function describes the autocorrelation of the PRN code,

$$\Lambda(\delta\tau) = \begin{cases} 1 - |\delta\tau|/\tau_c & \text{if} \quad |\delta\tau| \leq \tau_c(1 + \tau_c/T_i) \\ -\tau_c/T_i & \text{if} \quad |\delta\tau| > \tau_c(1 + \tau_c/T_i) \end{cases}, \tag{2}$$

where $\delta\tau(\tau, \vec{x})$ is the difference between τ and the delay of a signal reflected at the surface point $\vec{x}$, and τ_c is the PRN code chip length. The Doppler spreading function S describes the carrier-phase decorrelation with changing Doppler frequency,

$$S(\delta f) = \frac{\sin(\pi \delta f T_i)}{\pi \delta f T_i} \exp(-\pi i \delta f T_i), \tag{3}$$

where δf is the difference between f_C and the Doppler shift of a signal reflected at $\vec{x}$. R_t and R_r denote the distances from the surface point to the transmitter and the receiver, respectively, and σ_s^0 denotes the bistatic surface scattering coefficient.

2.1.3. Reflection Geometry, Range and Doppler Zones

For a sufficiently smooth surface (e.g., plain or ellipsoidal), there is a unique point of specular reflection. It fulfills the following specular

condition: The surface normal coincides with the bisector between incident and reflected signal ray. In other words, the angle between the surface normal and the bisector (the "scattering angle") is zero (cf. Figure 1).

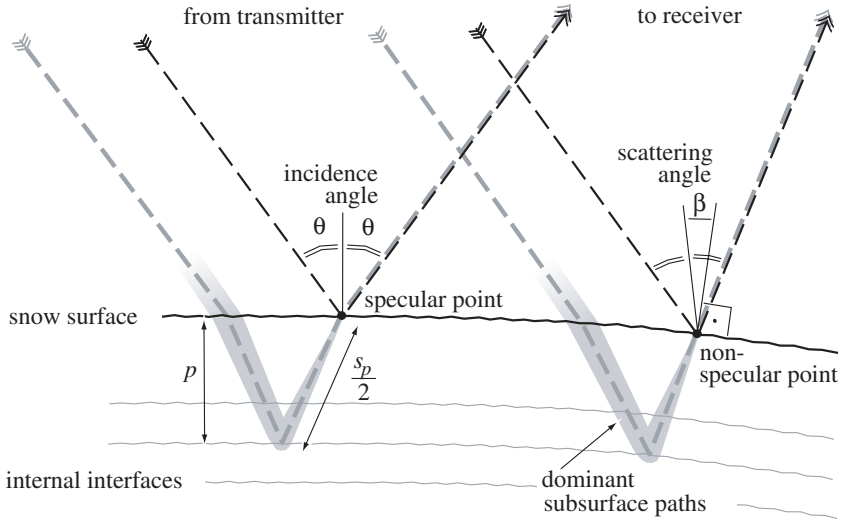

Figure 1. Geometry of surface reflection (black dashed lines) and volume reflection (gray dashed lines) for the specular and the non-specular situation.

A reflected signal's range delay (due to the signal path length) and Doppler frequency shift (due to the relative velocity between transmitter and receiver along the signal path) are functions of the surface reflection position $\vec{x}$. These functions are illustrated by equi-range and equi-Doppler lines [1]. Roughly, the lines of equal range delay are ellipses around the specular point, which is the point of minimum delay. The lines of equal Doppler frequency are hyperbolas. Examples will be simulated in Section 4.1.

The Λ^2 and $|S|^2$ functions in Equation (1) act like filters in delay and frequency that let pass only delays near τ and frequency shifts near f_C. They thus select signal contributions reflected from particular ground zones which are constrained by equi-range and equi-Doppler lines.

2.2. Ice Surface Reflection

We apply Equation (1) to describe surface reflections from an ice sheet. In contrast to ocean surfaces, the topographic variations on

ice sheets (with slopes of 1° and more) have considerable effects on the signal and are therefore taken into account. They affect not only the ranges and Doppler shifts of surface points but also the scattering coefficients which depend on the surface orientation relative to the signal's directions of incidence and reflection. Topographic variations are also important for the choice of the coherent integration time T_i and the time of incoherent averaging. To model the surface scattering coefficient we use the geometric optics limit of the Kirchhoff approximation (see Ulaby et al. [21] for the theory). Roughly speaking, the scattering coefficient is proportional to the probability of a surface facet to have the orientation of a specular reflector. This model is widely used for ocean applications of GPS reflections and proves itself for near-specular geometries and moderate grazing angles [20]. It has also been applied to scattering from ice at Ku-band [22] and L-band [23]. Little quantitative information is available on the highly variable surface structure of ice sheets (e.g., van der Veen et al. [24], Eickschen et al. [25], Herzfeld [26]), and some assumptions of geometric optics may not be strictly fulfilled — namely the assumption of a horizontal roughness scale larger than the wavelength scale. But for a first general attempt reasonable qualitative relations can be expected from this model.

2.3. Subsurface Reflection

In addition to surface reflection, penetration through the surface and reflections from subsurface have to be considered. Typically, the snowpack is composed of layers with the density varying from about $300\,\mathrm{kg/m^3}$ at the surface to $900\,\mathrm{kg/m^3}$ at about hundred meter depth. L-band microwaves largely penetrate this snowpack (see e.g., Rignot et al. [17]). Penetration depths around 100 meters can be expected.

2.3.1. Internal Layering as the Reflection Source

We assume that dielectric interfaces between firn layers are the internal reflection source for the L-band signal. Such layering structures are known to be the reflection source for P-band (lower frequency than L-band) ground penetrating radar [27] as well as for Ku-band (higher frequency) radar altimetry [28]. We consider density fluctuations as the main source of dielectric layering in the upper hundreds of meters. Fujita et al. [29] reported that density effects dominate in the upper 500 meters for a 179 MHz signal.

Roughness characteristics of internal interfaces are comparable to the surface [30]. Therefore the scattering at internal layering is

assumed to follow similar mechanisms as the surface reflection. Thus, internal scattering, too, is described by the geometric optics model.

2.3.2. Directivity Assumption and Uniformity Approximations

Typically, in the geometric optics model with small roughness, scattering is directive. That means, the reflected bistatic scattering has its maximum if the reflection geometry meets the specular condition, and decreases rapidly with deviation from the specular condition. For the scattering transmitted through an interface, the statement holds analogously with the condition of optical refraction. We will assume that the transition through the interfaces and the reflection at the interfaces are directive. Possibly occurring non-directive scattering could be understood as a source of noise in the modelled signal.

To allow a concise analytical modelling we will use two more approximations: First, the volume scattering will be factorised into a depth-dependent and a position-dependent factor. Thus, all laterally varying effects (like interface roughness, accumulation rate, firn transformation regime) must be covered by a single position-dependent factor. Second, in the evaluation of the signal path through the firn (but only there) we will neglect variations of incidence and reflection angles over the reflecting region and always apply the specular geometry (cf. Figure 1).

2.3.3. Analytical Model Derivation

Like the surface echo, we express the subsurface echo as an integral of contributions from all possible signal propagation paths. These contributions $V(\vec{x}, \tau_e)$ are distinguished by the surface point $\vec{x}$ at which the signal path "leaves" the firn and the excess travel time τ_e. This τ_e is the travel time difference between the volume-reflected signal V and a surface signal reflected at $\vec{x}$. Hence we express the waveform of the subsurface signal, $W_v(\tau, f_C)$, by

$$W_v(\tau, f_C) = \frac{T_i^2}{4\pi} \int_{\vec{x}} \int_{\tau_e} V(\vec{x}, \tau_e) d\tau_e dA(\vec{x}). \tag{4}$$

The directivity assumption formulated above now means that the parameters $\vec{x}$ and τ_e determine an approximate signal path (with an approximate depth of reflection p) that dominates the contribution $V(\vec{x}, \tau_e)$. For illustration, Figure 1 shows shaded corridors of dominant signal paths for respective parameters $\vec{x}$ and τ_e.

The subsurface contribution $V(\vec{x}, \tau_e)$ is determined by the antenna and receiver functions $D^2\Lambda^2|S|^2$ (cf. Equation (1)), by the propagation

between the antennas and the snow surface, the transition through the firn-air interface, the transfer through the firn and the reflective scattering at the firn layering structure. We evaluate these constituents now: The functions $D^2\Lambda^2|S|^2$ act in the same way as for the surface signal. Only the excess travel time has to be regarded in the Λ evaluation: $\Lambda = \Lambda(\delta\tau(\vec{x},\tau) - \tau_e) = \Lambda(\delta\tau(\vec{x},\tau - \tau_e))$ where $\delta\tau$ is calculated for surface reflection at $\vec{x}$ like in Section 2.1. The propagation loss between the antennas and the snow surface can be approximately expressed by the distances R_t and R_r from $\vec{x}$ to transmitter and receiver. The transmissions through the snow surface are described by the transmissivity $(1 - \Gamma_s)$ with the surface reflectivity Γ_s. The loss factor L upon signal transfer through the firn will be evaluated by the radiative transfer method. Finally, the scattering in the firn region contributing to $V(\vec{x},\tau_e)$ is expressed by the volume scattering coefficient σ_v^0 (defined as scattering coefficient per meter depth). To relate σ_v^0 (which is related to incremental depth) to incremental signal propagation time, as needed in Equation (4), the derivation of reflection depth to excess travel time, $dp/d\tau_e$, is multiplied. Hence we have

$$V(\vec{x},\tau_e) = D^2\Lambda^2|S|^2 R_t^{-2} R_r^{-2} (1-\Gamma_s)^2 L^{-1} \sigma_v^0 \frac{dp}{d\tau_e}. \tag{5}$$

At this point we apply the uniformity approximations explained above. We model σ_v^0 by the factorization

$$\sigma_v^0(\vec{x}, p(\tau_e)) = \sigma_s^0(\vec{x})\sigma_{v/s}^0(p(\tau_e)). \tag{6}$$

The surface scattering coefficient σ_s^0 accounts for lateral variations (due to the varying scattering geometry and varying interface roughness conditions), whereas the factor $\sigma_{v/s}^0$ accounts for scattering variations with depth. Further we consider the magnitudes L and $dp/d\tau_e$ independent of $\vec{x}$.

In result, Equation (4), with a changed order of integration, reads

$$W_v(\tau, f_C) = \int_{\tau_e} (1-\Gamma_s)^2 L^{-1} \frac{dp}{d\tau_e} \sigma_{v/s}^0 \left(\frac{T_i^2}{4\pi} \int_{\vec{x}} D^2\Lambda^2|S|^2 R_t^{-2} R_r^{-2} \sigma_s^0 dA(\vec{x}) \right) d\tau_e. \tag{7}$$

The bracketed expression has the structure of (1) but with a shifted delay dependence of Λ: Now, $\Lambda = \Lambda(\delta\tau(\vec{x},\tau - \tau_e))$. Hence (7) means that the volume echo

$$W_v(\tau, f_C) = Z * W_s \tag{8}$$

is a convolution with respect to τ of the surface echo $W_s(\tau, f_C)$ and a volume function

$$Z(\tau_e) = (1 - \Gamma_s)^2 L^{-1}(\tau_e) \frac{dp}{d\tau_e}(\tau_e) \sigma^0_{v/s}(p(\tau_e)). \tag{9}$$

2.4. Evaluation of Model Parameters

We now explain in more detail how the model parameters are evaluated for the simulation studies. The formulas are understood with SI units, and kg/m^2 p.a = mm w.e. p.a. for accumulation rates.

2.4.1. Surface Scattering

The surface scattering coefficient σ^0_s is computed under the assumption of an isotropic Gaussian roughness characterised by the rms roughness slope σ_{sl}. It is hence given by

$$\sigma^0_s = \frac{\Gamma_s}{2\sigma^2_{sl} \cos^4 \beta} \exp\left(-\frac{\tan^2 \beta}{2\sigma^2_{sl}}\right) \tag{10}$$

with Γ_s the surface reflectivity (set to 0.017), and β the scattering angle (cf. Figure 1) [31].

Topographic heights are taken from the altimetric model of Antarctica by Rémy et al. [32]. Its resolution is 2.5 km. Height variations of smaller horizontal scale are treated as roughness.

For a reasonable evaluation of the rms roughness slope σ_{sl} affecting L-band reflections, the lack of empirical data leads to a heuristic approach. Legrésy and Rémy [28] discussed that the leading edge parameter T_r of radar altimeter waveforms varies depending on the meter to kilometer scale surface roughness. We take these variations to qualitatively represent roughness variations for L-band reflections. We choose the arbitrary relation $\sigma_{sl} = -0.01 + 0.04 T_r$ to generate maps of σ_{sl} ranging from 0.01 to larger than 0.15.

2.4.2. Subsurface Scattering

To evaluate the volume scattering coefficient σ^0_v, we consider the incoherent combination of reflections from internal density contrasts. We do not account for neither the influence of the temperature regime on stratification nor for possible coherence effects in this simple approach. Scattering variations are basically represented as depending on accumulation rate variations.

We assume two density contrasts per annual deposition leading to a number of $d_i = 2\rho/a$ interfaces per meter, with ρ the density, and

a the annual accumulation rate taken from Vaughan et al. [14]. We assume an exponential decrease of the density contrasts $\delta\rho$ with depth p, setting $\delta\rho(p) = 50\exp(-0.016p)$. This gives density contrasts of $50\,\mathrm{kg/m^3}$ near the surface in agreement with the order of magnitude reported in field measurements [33–35], and density contrasts of $10\,\mathrm{kg/m^3}$ in 100 m depth in agreement with an estimation in Robin et al. [36]. A density contrast $\delta\rho$ gives a reflectivity $\Gamma = 5.76\cdot10^{-8}\delta\rho^2$ for normal incidence [36] and, in sufficient approximation, also for the non-normal incidences considered here. In result we find $\sigma^0_{v/s} = \sigma^0_v/\sigma^0_s = 2.88\cdot10^{-4}\rho a^{-1}\Gamma_s^{-1}\exp(-0.032p)$.

We note that this is certainly not an accurate description of the snowpack echo as seen by the L-band signal, but it shall give a resonable qualitative representation. A better description will be possible when measurements are available.

2.4.3. Signal Path through Firn

For a simple evaluation of the signal path parameters needed in the volume function Z, the firn density is approximated everywhere by a mean value of $\rho = 600\,\mathrm{kg/m^3}$ leading to a refractive index $n = 1 + 0.85\cdot10^{-3}\rho = 1.51$ [27].

Then, with the optical law of refraction at the snow surface, simple geometric relations for the subsurface signal path can be derived for specular geometry (cf. Figure 1): With c denoting the vacuum speed of light and θ the incidence angle, the depth of reflection can be computed to be $p = \frac{1}{2}\tau_e c n^{-1}(1 - n^{-2}\sin^2\theta)^{-1/2}$, which implies $dp/d\tau_e = \frac{1}{2}cn^{-1}(1 - n^{-2}\sin^2\theta)^{-1/2}$, and the path length within the firn can be computed as $s_p = \tau_e c n^{-1}(1 - n^{-2}\sin^2\theta)^{-1}$. Note for these computations that, for $\theta \neq 0$, not only the travel time within the firn but also the travel time between transmitter and snow surface changes with excess travel time τ_e.

The absorption coefficient is given by Matzler [37] as $\kappa_a = 2\pi f\epsilon''/(c\sqrt{\epsilon'})$, with f the frequency and $\epsilon' - i\epsilon''$ the dielectric constant. Substituting expressions for ϵ' and ϵ'' given by Tiuri et al. [38] leads to $\kappa_a = (0.0118 + 1.454\cdot10^{-16}f^{3/2})\exp(0.036(T-273))$ for the chosen density value. The temperature T is taken from Drewry [39]. The loss by scattering (both at internal interfaces and at individual ice grains) can be found negligible compared to absorption loss. Hence, the loss factor L is given by the absorption along the propagation path, $L = \exp(\kappa_a s_p)$.

If necessary, the radiative transfer relations can be generalised to account for density variations.

3. NUMERICAL SIMULATIONS

3.1. General Approach

We have developed software tools to simulate the signal arising from GPS reflections on ice sheets. Since the reflection signal and possible applications still have to be analysed and detailed measurement and processing schemes still have to be defined, we attempt to output the full information that is potentially recordable within the used approach. Thus, more information is recorded than in any realistic measurement scenario in order to allow a detailed understanding of the signal and to study various measurement and processing schemes. We also remark that the simulation software is sufficiently general and modular to be adapted even for the study of different bistatic techniques such as the interferometric cartwheel mission [40].

While being very general, the simulations are also ideal with respect to noise. Noise is not considered here, and we use an omnidirectional antenna pattern for simplicity. But the signal-to-noise ratio is of course a crucial issue for GNSS reflection applications especially from space (see e.g., Caparrini [41] for a discussion of antenna requirements). So, when specific configurations of measurement geometry and hardware are considered, the simulated signal powers have to be analysed in conjunction with respective energy budgets and noise characteristics.

The main simulation outputs are the Delay-Doppler waveforms. The span of delay and frequency values and their resolution are chosen to give a comprehensive description of the reflection signal. In addition to the waveforms, auxiliary information is provided, such as the range and Doppler zones and scattering coefficients on the ground.

3.2. Simulation Description

For the given transmitter and receiver positions of a measurement, first, the nominal specular point is computed. This is the specular point with respect to a reference surface (the reference earth ellipsoid for the satellite case and a horizontal surface at local topographic height in the airplane case).

Around the nominal specular point, a suitable local surface grid is defined to represent the "reflecting region". For the satellite case we choose an area of 250 km ("view direction") times 200 km (across "view direction"), and for the airplane case we scale it down to 2.5 km times 2 km according to the receiver height proportion. As horizontal resolution we take 62.5 m and 5 m for the satellite and the airplane case, respectively, as a compromise between computing time and numerical

noise.

The local grid is used for the numerical integral of Equation (1). For preparation, the surface topography and the surface roughness are interpolated to the grid from the data sources explained in Section 2.4. The surface scattering coefficient σ_s^0 is computed from the roughness and the local reflection geometry (arising from the transmitter-receiver constellation and the topographic slopes). The signal scaling due to transmitter and receiver distances and antenna gain is computed. Finally, the range delay and the Doppler frequency shift of a reflection upon every grid element are computed.

The entire surface waveform is now computed in a single integration loop over the surface grid: For all grid elements, their power contributions to the receiver input are assigned to their range and frequency bins and summed up separately in every bin. The resulting intermediate product gives the receiver input per range and frequency increment and is still independent of the receiver-inherent filter functions. It is then convolved with the Λ^2 and $|S|^2$ functions to give the receiver-output delay-Doppler waveform for the surface echo.

For the volume echo, the volume function Z is evaluated as explained in Section 2.4. It is then convolved in the range domain to the surface waveform. The result is the delay-Doppler waveform of the volume echo.

Based on the simulated waveforms and some auxiliary data, various measurement and processing techniques can be investigated, such as the overflight focussing described later in Section 4.4.

4. RESULTS

4.1. Simulated Measurement Scenarios

We present simulations of airborne and spaceborne measurements over Antarctica. Figure 2 shows the geographic situation of the spaceborne measurements with a satellite crossing the continent at 400 km height. Regions around the specular point that are considered for echo contributions ("reflecting regions") are shown for every third measurement along the track. We choose measurement M9 for the example studies. Some parameters of this measurement are also given in the figure. The airborne measurements are simulated for an airplane flying at 200 m/s speed and 4 km height above snow surface. Their geometry is arranged in a way that the nominal specular points (cf. Section 3.2) are the same as for the satellite simulations.

For the presented simulations we use the P-Code PRN signal with 30 m "chip length" on the 1.58 GHz L1 carrier. The correlation time T_i is 1 ms and the antenna gain is set to 1.

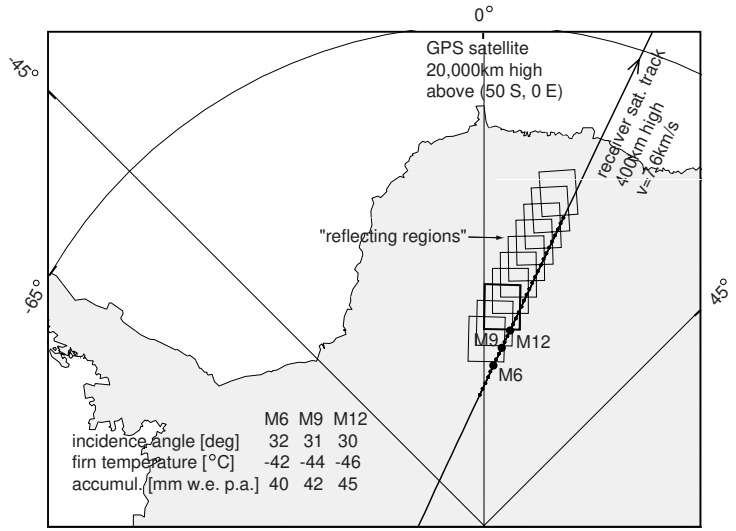

Figure 2. Geographic situation of the simulations. Receiver positions of measurements every 5 seconds are indicated by circles along the satellite track. Regions considered for echo contributions ("reflecting regions") are shown for every third measurement, i.e., every 15 seconds.

The equi-range and equi-Doppler lines for measurement M9 are shown in Figure 3 (left) for the airplane and the satellite scenario. One can see that Doppler frequency spreading is negligible for airplane velocities but essential in the satellite case. The span of range delays is proportional to the receiver height and thus much larger for the satellite measurement. Figure 3 (right) shows the input surface topography and roughness.

4.2. Qualitative Studies with Idealised Interfaces

For a clearer illustration of general phenomena we first present simulations for idealised air-firn and internal interfaces. We take the area in Figure 3 but set the surface height and the rms roughness slope to a constant value (the value of the specular point).

4.2.1. Waveform Shape

The resulting simulated delay-Doppler waveforms are shown in Figure 4 for the pure surface echo (left) and the combined surface-volume echo (right). They will serve as reference for successive simulations. Let us recall some general waveform characteristics:

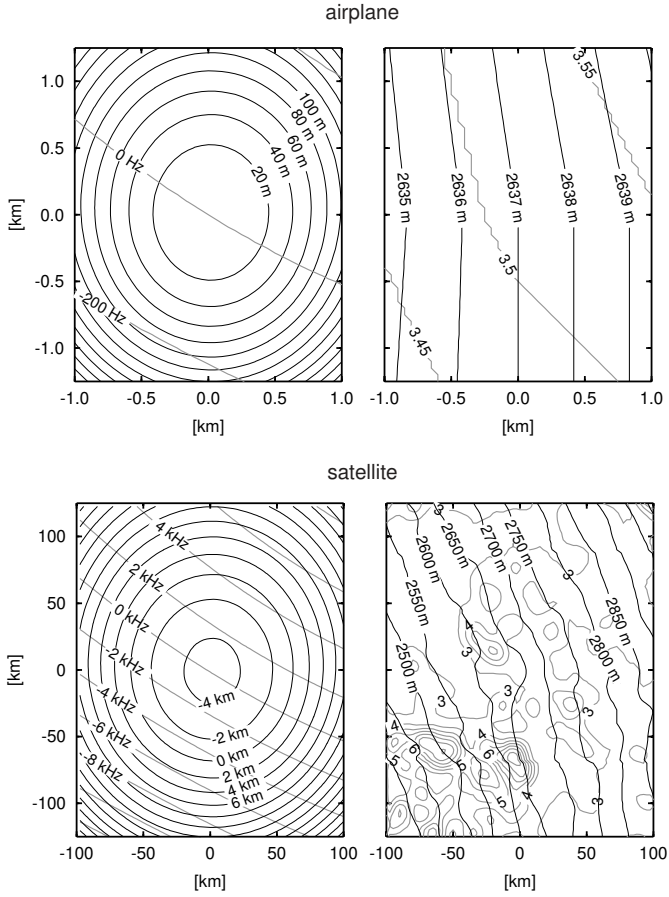

Figure 3. "Reflecting regions" for measurement M9 (cf. Figure 2 and Section 3.2). Airplane case (top) and the satellite case (bottom). Left: equi-range lines (black) and equi-Doppler lines (gray). Range delay and frequency shift are centered in the nominal specular point. Note the different contour intervals. Right: surface topography (black) and rms roughness slope with unit 10^{-2} (gray).

As it is clear from Figure 3, the span of ranges and frequencies is much larger for the satellite case than for the airplane case. The peak power, at the other hand, is substantially lower for the satellite case. This is due to the signal's spreading over range delay and frequency shift and due to higher propagation losses.

The frequency-width of the waveform in the airplane case is due

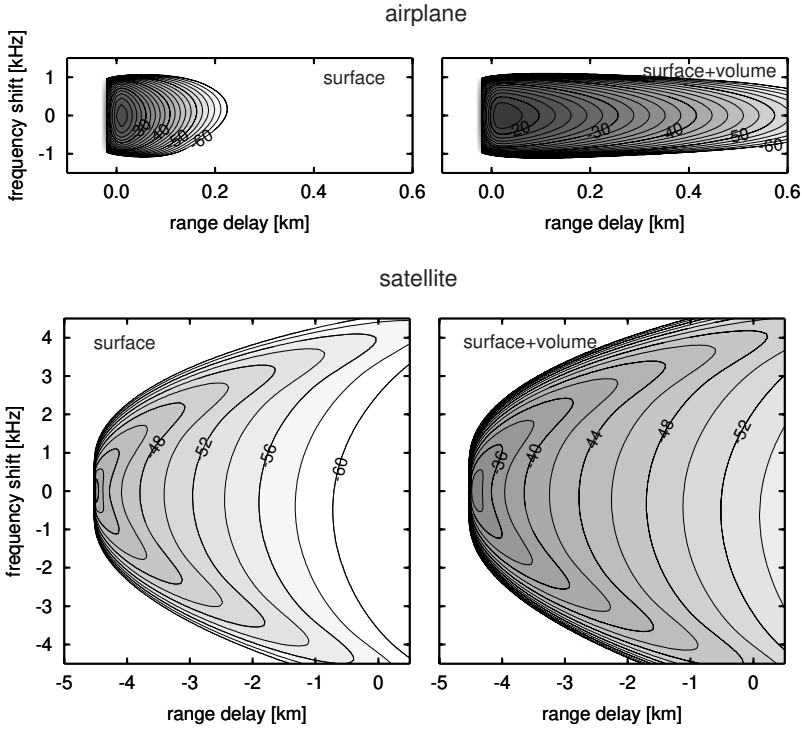

Figure 4. Delay-Doppler waveforms for measurement M9 with idealised interfaces. Power is shown in dB normalised to the direct signal power. Range delay and frequency shift are centered in the nominal specular point. Left: surface echo. Right: combined surface and volume echo. These simulations are taken as the reference for Figures 7 and 8.

to the Doppler spreading function $|S|^2$ of Equation (1). In contrast, for the satellite case, the waveform's frequency shape is primarily due to the Doppler variations over the reflecting ground region and gives a means to distinct different contributions. The surface echo waveform vertex (i.e., the region around −4.5 km range delay and 0 kHz frequency shift) originates from the vicinity of the specular point. Waveform parts "behind" the vertex (i.e., with equal frequency but larger delay) originate from intersections of the specular point's Doppler zone with range zones of higher delays. For frequencies apart from the specular point's frequency, the signal arises only at larger range delays, because the respective Doppler zones do not intersect with the smallest range zones.

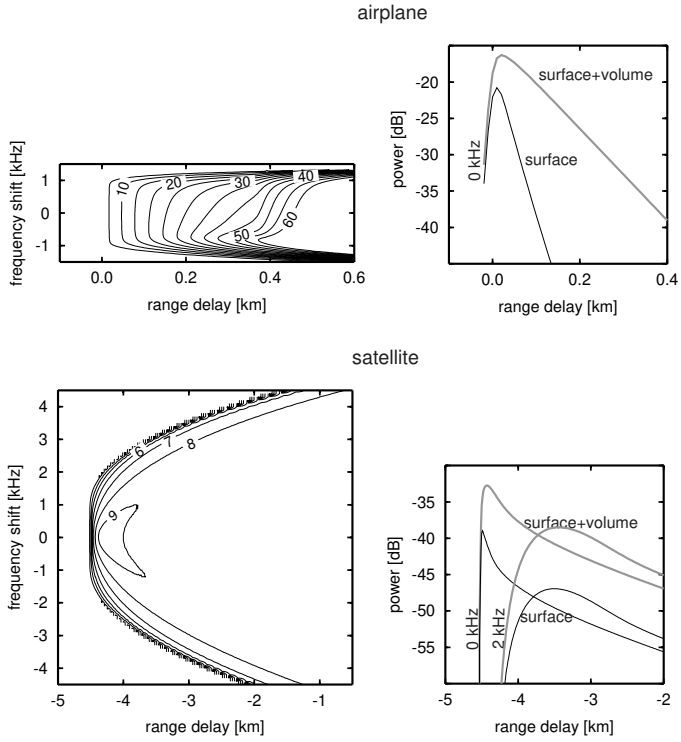

Figure 5. Comparison between combined surface-volume echo and pure surface echo. Left: Quotient between combined waveform and pure surface waveform in dB. Right: range-power curves for fixed frequency shifts: pure surface (black) and combined signal (gray).

For a fixed frequency, the range-power curves are similar to the radar altimeter waveforms with a relatively short leading edge and a longer trailing edge (cf. also Figure 5, right).

The surface height determines the absolute range of the entire waveform (see the satellite case where the range delay refers to the reference ellipsoid). Altimetric applications, however, would have to overcome among other things the coarse resolution due to the chip length.

4.2.2. Effect of Subsurface Contribution

The effect of the subsurface contribution can be seen in Figure 5 where the combined surface-volume signal is compared to the pure surface signal. The volume contribution is clearly dominant in the combined

signal.

For the airborne case, the presence of volume echo changes the waveform shape: The pure surface echo is concentrated to a narrow range span. By the volume echo, it is reproduced from depth (i.e., larger range) according to the volume function. So the trailing edge now reflects the volume function.

For the satellite case, in contrast, the presence of volume echo does not change the overall waveform shape: the proportion between combined signal and surface-only signal is nearly constant. This is because the volume function is relatively short in the delay dimension and so its convolution acts like a constant multiplication. However, at the crest, the waveform shape is changed by the volume echo: The maxima are shifted towards larger delays, and the shape at the waveform vertex is changed characteristically from a relatively sharp peak to a smoother maximum.

The exact effect of the subsurface contribution naturally depends on the particular volume function Z. The variability of Z with respect to its main parameters is illustrated in Figure 6: Firn temperature affects the absorption, and therefore mainly the contributions from deep reflections. The incidence angle's influence is complex but small. Important effects come from accumulation variations which represent volume scattering variations in our model.

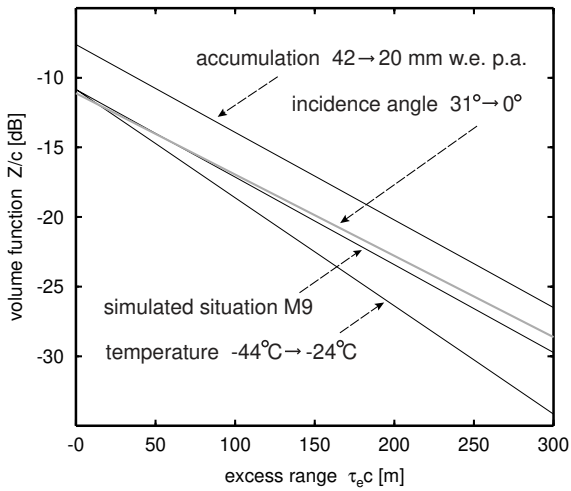

Figure 6. Volume function Z: sensitivity to its parameters. Z is shown (scaled by the speed of light) for the simulated situation of measurement M9 and for three other situations with changed values for accumulation, incidence angle and temperature, respectively.

4.2.3. Effect of Roughness

To demonstrate the influence of surface and internal interface roughness, the above simulation of measurement M9 is repeated with a smoother surface: The rms roughness slope is changed from 0.035 to 0.02. Figure 7 shows the resulting waveforms (left) and their comparison to the original simulation (right).

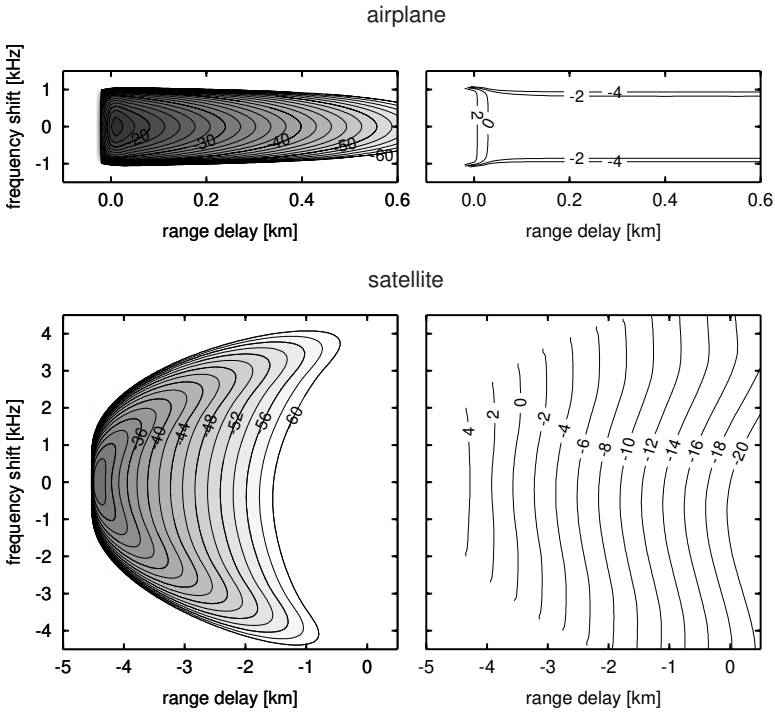

Figure 7. Effect of roughness: Left: waveforms for the situation of Figure 4 (right) except that the rms roughness slope is decreased from 0.035 to 0.02. Right: Quotient [dB] of the waveforms on the left to the waveforms of Figure 4 (right).

The roughness decrease increases the power scattered from the vicinity of the specular point, forming the waveform vertex. Also, in the spaceborne case, the trailing edge is now steeper because the scattered power decreases more rapidly when the reflection geometry deviates from the specular geometry. This effect is considered over oceans to measure the sea roughness [9]. In the airborne case, for our simulation, the trailing edge shape is predominantly due to the volume function (see above) and is thus insensitive to roughness effects.

4.3. Account for Topographic and Roughness Variations

We now apply the variations in topography and roughness within the "reflecting region" (cf. Figure 3). Figure 8 (left) shows the resulting waveforms and Figure 8 (right) shows their comparison to the previous simulations with idealised interfaces.

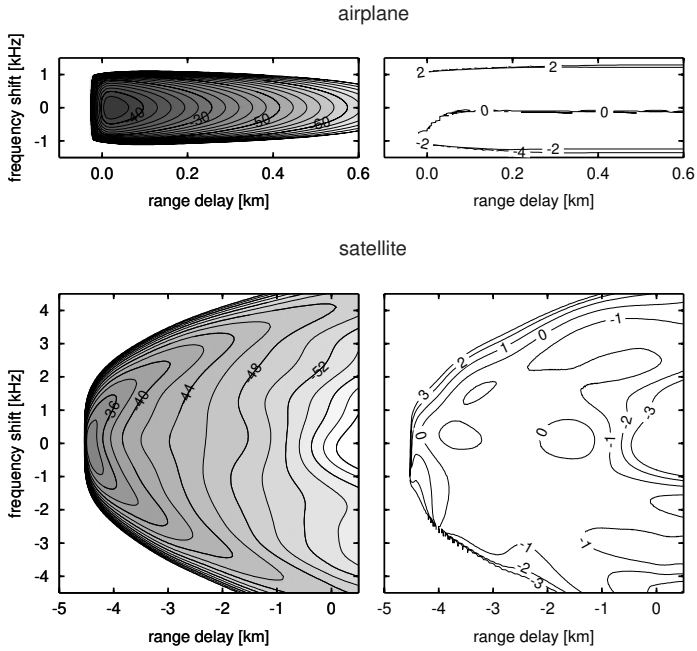

Figure 8. Effect of topographic and roughness variations: Left: waveforms for measurement M9 (cf. Figure 2), now with account for topographic and roughness variations. Right: Quotient [dB] of the waveforms on the left to the waveforms for constant topography and roughness (Figure 4, right).

The ideal waveform shapes obtained for constant topography and roughness are now perturbed by the effect of topography and roughness variations. The present topographic slope makes the higher frequency contributions arrive earlier and the lower frequency contributions arrive later than for a horizontal surface. This leads to a shift of the entire waveform towards higher frequencies. The smaller-scale variations within the waveform (spaceborne case) are predominantly due to roughness variations. For a more representative picture of the signal variations along the satellite track, Figure 9 shows the 0 kHz range-power relations along the whole track of Figure 2.

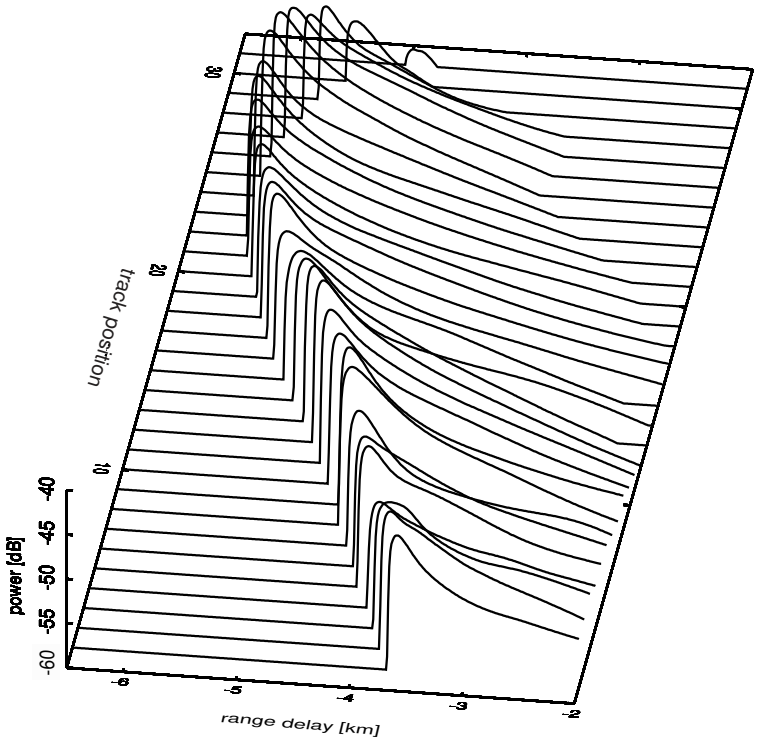

Figure 9. Signal variations along the satellite track of Figure 2: the range-power relations at 0 kHz frequency shift are shown for the measurements every 5 seconds along the track.

4.4. Focussing on Subzones

4.4.1. Concept of Focussing on Subzones During a Satellite Pass

So far we have analysed how single measurements are composed of contributions from extended surface and subsurface regions. Now we consider that, in the spaceborne case, single ground areas contribute to many successive measurements during a receiver pass and could therefore be observed repeatedly.

In general, surface scattering elements can not be uniquely distinguished by their delay and Doppler values. Only the points of tangency between equi-range and equi-Doppler lines have unique pairs of delay and Doppler values. It can be further shown that the line of these tangent points is oriented in the direction of the receiver velocity (see Figure 10 left). So, surface points with a unique pair of delay and

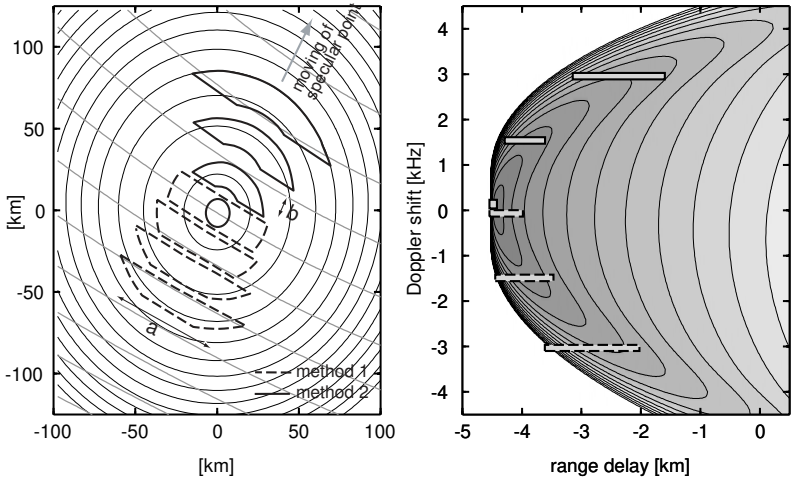

Figure 10. Left: scheme of surface subzones that can be focussed on by extracting appropriate waveform parts (2 methods are shown where method 1 keeps the length a constant and method 2 keeps the length b constant). Right: the waveform parts corresponding to the surface subregions. (2 methods).

Doppler values preserve their uniqueness property along a receiver pass. Thus, the scattering from the vicinity of these points can be monitored in a series of measurements under changing reflection geometry.

Such a measurement series could contain roughness information, since interface roughnesses affect the way in which scattering changes with geometry. Further, we have seen in Section 4.2 that the combinations of surface and volume contributions are different for different parts of the waveform, or in other words, for different reflection geometries. Therefore, successive observations of a subregion can also give indications about the subsurface contribution.

4.4.2. Focussing Procedures

We have derived formalisms to relate special waveform parts to special surface subzones such that a waveform part contains surface echoes only from its related subzone. The computations are based on a second order Taylor development for the range and Doppler values of surface points with respect to the nominal specular point. Figure 10 shows a scheme of the considered ground subzones and the respective waveform parts. Among the two methods presented there we consider results of method 2 in the following.

For a selected ground subzone, we can integrate the power of the related waveform part and divide it by the subzone area to obtain the scattering coefficient. We can do this scattering coefficient computation for successive measurements during a satellite receiver pass, selecting always subzones that refer to a fixed ground position. So we obtain the scattering of a fixed ground region under the changing reflection geometry during a satellite receiver pass. The result of such a focussing procedure is a ground region's scattering coefficient with respect to the scattering angle β (cf. Figure 1). We show examples for two positions with different roughnesses. They are observed during a 20 second receiver pass with simulated measurements every second.

Figure 11 shows the obtained scattering coefficients for a simulation with the pure surface signal and a simulation with the combined surface-volume signal. For the surface signal, the obtained relation between scattering angle and scattering coefficient recovers the model relation (shown as dashed line) which was used in the simulation. The rms roughness slope which determines this relation could be inferred from the obtained data. The scattering coefficient obtained from the combined surface-volume signal appears proportional to surface scattering, except for low scattering angles, i.e., for near-specular geometry, where it decreases remarkably. This is plausible from the following observation (cf. Section 4.2): For non-specular surface positions, the surface contribution is overlapped by a proportional volume contribution with the same delay and Doppler values. Only for the specular surface signal, having the minimum range, there is no proportional overlap of volume signals.

The two curves in Figure 11 that show quotients of different scattering coefficient curves illustrate the different effects of roughness and subsurface contribution: A change in roughness changes the decrease and the shape of the entire functions. A subsurface contribution increases the entire function and changes its shape essentially only near zero scattering angle. Thus, under the conditions of our simulation, the rms roughness slope in a ground subregion could be inferred if the obtained scattering coefficients are analysed for, say, $\beta \geq 0.02$. Moreover, since surface and volume signals give qualitatively different results, the focussing procedure can give indications about the quantity of volume echo. We finally remark that the possibility to distinguish surface and volume contributions is based on the different surface and volume waveform shapes near the vertex. A further analysis of this waveform part could give more information about subsurface scattering.

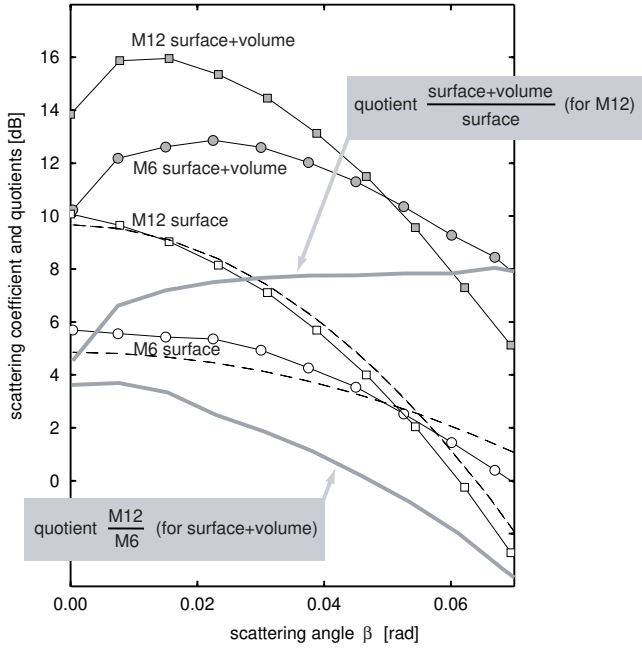

Figure 11. The scattering coefficient as a function of scattering angle: simulated results of the focussing procedure. For two ground subzones (around the central positions of measurements M6 and M12 with rms roughness slopes 0.053 and 0.027), the relations are obtained both for the surface signal and the combined surface-volume signal. For the surface signal, the model relations are added as dashed lines. To highlight the sensitivity to roughness and to the surface-volume proportion, we also show the quotients between the two positions (i.e., different roughnesses) and between the surface-volume and the pure-surface signal.

5. CONCLUSIONS

The use of reflected GNSS signals for remote sensing is attractive due to the high resolution in space and time, the potentially low cost and the peculiar bistatic, forward scattering geometry which is complementary to the geometry of other techniques. Our studies suggest that it is worth to further persue potential applications for ice sheet remote sensing.

We have derived a model for GPS signal reflections from a rough and penetrating medium and have applied it to an ice sheet. We have developed software tools to simulate the GPS reflection signal that

can be potentially recorded in airborne and spaceborne measurements. This provides a basis to understand the complex relationships affecting the signal and to further investigate it.

Little is known about the non-vertical forward-scattering of L-band microwaves from ice sheets. Hence, our model is heuristic and attempts to describe a reasonable qualitative behaviour. It adapts knowledge from the "neighbouring" frequency bands of radar altimetry and ground penetrating radar. With more empirical data an improved modelling will be possible. Constraints by noise depending on antenna and receiver realisations are another open issue. Hence it is early to define detailed measurement and processing techniques for particular applications. Our modelling and our simulations are therefore general enough to serve as a starting point for studying of various measurement and processing strategies.

While altimetric applications are questionable, our studies show how the signal is sensitive to the roughness of the snow surface (together with internal interfaces) and to firn parameters like accumulation rates and internal density fluctuations. To benefit from these sensitivities in spaceborne measurements, the complexity of the signal suggests to use the delay and Doppler structure for a focussing on ground subzones. We have implemented a procedure to observe the scattering from particular ground zones under the changing reflection geometry occurring during a satellite pass. Simulation results for this procedure indicate the potential to separately infer parameters linked to interface roughnesses and to firnpack characteristics.

Future GNSS reflection measurements could be analysed in conjunction with complementary microwave applications, in particular with different L-band measurements, such as the passive SMOS mission [42], the ALOS mission [43], or the interferometric cartwheel mission [40] if run with an L-band companion SAR. Relating the measurements to accumulation rates, and hence improving millenium-scale accumulation maps could be a possible and very attractive application. Since the firn in tens to hundreds of meters depth is not subject to short-term and interannual variations, GNSS reflection measurements can be collected in any time regime to infer firn properties of these depths. Thus, any opportunity is welcome to gather empirical GNSS reflection data over ice sheets, possibly as a secondary objective of a GNSS reflectometry mission.

ACKNOWLEDGMENT

This research was funded by the German Research Foundation (DFG) under grant Di 473/5-1, 5-2. Travelling support was provided by

the German Academic Exchange Service (DAAD) in the frame of the PROCOPE program under grants D/0122863 and F/02598YA.

REFERENCES

1. Martin-Neira, M., "A passive reflectometry and interferometry system (PARIS): Application to ocean altimetry," *ESA Journal*, Vol. 17, 321–355, 1993.
2. Auber, J.-C., A. Bilbaut, and J. M. Rigal, "Characterization of multipath on land and sea at GPS frequencies," *Proc. Inst. Navigation ION-GPS-94 Conf.*, Part 2, 1155–1171, Paris, France, 1994.
3. Lowe, S. T., G. Hajj, J. Labrecque, L. Romans, L. Young, and C. Zuffada, "LEO detection of an ocean-reflected GPS signal," *Proc. GPS Surface Reflections Workshop at Goddard Space Flight Center*, JPL, Pasadena, CA, July 1998.
4. Garrison, J. L., S. J. Katzberg, and M. I. Hill, "Effect of sea roughness on bistatically scattered range coded signals from the Global Positioning System," *Geophys. Res. Lett.*, Vol. 25, No. 13, 2257–2260, 1998.
5. Martin-Neira, M., M. Caparrini, J. Font-Rossello, S. Lannelongue, and C. S. Vallmitjana, "The PARIS concept: An experimental demonstration of sea surface altimetry using GPS reflected signals," *IEEE Trans. Geosci. Remote Sensing*, Vol. 39, No. 1, 142–150, 2001.
6. Treuhaft, R. N., S. T. Lowe, C. Zuffada, and Y. Chao, "2-cm GPS altimetry over Crater Lake," *Geophys. Res. Lett.*, Vol. 28, No. 23, 4343–4346, 2001.
7. Lowe, S. T., C. Zuffada, Y. Chao, P. Kroger, and L. E. Young, "5-cm precision aircraft ocean altimetry using GPS reflections," *Geophys. Res. Lett.*, Vol. 29, No. 10, 2002.
8. ESA, "A GPS-based ocean altimetry experiment at ESTEC," *ESA Bulletin*, Vol. 101, 133–134, 2000.
9. Garrison, J. L., A. Komjathy, V. U. Zavorotny, and S. J. Katzberg, "Wind speed measurement using forward scattered GPS signals," *IEEE Trans. Geosci. Remote Sensing*, Vol. 40, No. 1, 50–65, 2002.
10. Born, G., A. Komjathy, P. Axelrad, and S. Crumpton, "Towards ingesting ionospheric data of surface reflected GPS signals into global ionospheric models," *Ionospheric Determination and Specification for Ocean Altimetry and GPS Surface Reflection Workshop*, JPL, Pasadena, CA, December 1997.

11. Kavak, A., W. J. Vogel, and G. Xu, "Using GPS to measure ground complex permittivity," *Electronics Letters*, Vol. 34, No. 5, 254–255, 1998.
12. Komjathy, A., J. Maslanik, V. U. Zavorotny, P. Axelrad, and S. J. Katzberg, "Sea ice remote sensing using surface reflected GPS signals," *IEEE 2000 Intern. Geosci. Remote Sensing Symposium*, Honolulu Hawaii, July 24–28, 2000.
13. Beyerle, G., K. Hocke, J. Wickert, T. Schmidt, C. Marquardt, and Ch. Reigber, "GPS radio occultations with CHAMP: A radio holographic analysis of GPS signal propagation in the troposphere and surface reflections," *J. Geophys. Res.*, (D), 2002 (in print).
14. Vaughan, D. G., J. L. Bamber, M. Giovinetto, J. A. Russell, and P. R. Cooper, "Reassessment of net surface mass balance in Antarctica," *J. Climate*, Vol. 12, 933–946, 1999.
15. Winnebrenner, D. P., R. J. Arthern, and C. A. Shuman, "Mapping Greenland accumulation rates using observations of thermal emission at 4.5-cm wavelength," *J. Geophys. Res.*, Vol. 106, No. D24, 33,919–33,934, 2001.
16. Drinkwater, M. R., D. G. Long, and A. W. Bingham, "Greenland snow accumulation estimates from satellite radar scatterometer data," *J. Geophys. Res.*, Vol. 106, No. D24, 33,935–33,950, 2001.
17. Rignot, E., K. Echelmeyer, and W. Krabill, "Penetration depth of interferometric synthetic-aperture radar signals in snow and ice," *Geophys. Res. Lett.*, Vol. 28, No. 18, 3501–3504, 2000.
18. Parkinson, B. W. and J. J. Spilker, Jr., *Global Positioning System: Theory and Applications*, American Institute of Aeronautics and Astronautics, Inc., Boston, 1996.
19. Seeber, G., *Satellite Geodesy*, Walter de Gruyter, Berlin, 1993.
20. Zavorotny, V. U. and A. G. Voronovich, "Scattering of GPS signals from the ocean with wind remote sensing application," *IEEE Trans. Geosci. Rem. Sensing*, Vol. 38, No. 2, 951–964, 2000.
21. Ulaby, F. T., R. K. Moore, and A. K. Fung, *Microwave Remote Sensing*, Vols. 1,2,3, Addison-Wesley, London, 1982, 1983, 1986.
22. Femenias, P., F. Remy, R. Raizonville, and J. F. Minster, "Analysis of satellite-altimeter height measurements above continental ice sheets," *J. Glaciol.*, Vol. 39, No. 133, 591–600, 1993.
23. Jezek, K. C., M. R. Drinkwater, J. P. Crawford, R. Bindschadler, and R. Kwok, "Analysis of synthetic aperture radar data collected over the southwestern Greenland ice sheet," *J. Glaciol.*, Vol. 39, No. 131, 119–132, 1993.

24. van der Veen, C. J., W. B. Krabill, B. M. Csatho, and J. F. Bolzan, "Surface roughness on the greenland ice sheet from airborne laser altimetry," *Geophys. Res. Lett.*, Vol. 25, No. 20, 3887–3890, 1998.
25. Eickschen, S. and M. A. Lange, "First results of ice surface classification as an approach for a better determination of radar altimeter derived ice shield topography," *EOS*, 79, 1998. Fall Meet. Suppl., Abstract H11B-21.
26. Herzfeld, U. C., H. Mayer, W. Feller, and M. Mimler, "Geostatistical analysis of glacier-roughness data," *Ann. Glaciol.*, Vol. 30, 235–242, 2000.
27. Bogorodsky, V. V., C. R. Bentley, and P. E. Gudmandsen, *Radioglaciology*, D. Reidel Publishing Company, Dordrecht, 1985.
28. Legrésy, B. and F. Rémy, "Altimetric observations of surface characteristics of the Antarctic ice sheet," *J. Glaciol.*, Vol. 43, No. 144, 265–275, 1997.
29. Fujita, S., H. Maeno, S. Uratsuka, T. Furukawa, S. Mae, Y. Fujii, and O. Watanabe, "Nature of radio echo layering in the Antarctic ice sheet detected by a two-frequency experiment," *J. Geophys. Res.*, Vol. 104, No. B6, 13,013–13,024, 1999.
30. Alley, R. B., "Concerning the deposition and diagenesis of strata in polar firn," *J. Glaciol.*, Vol. 34, No. 118, 283–290, 1988.
31. Barrick, D. E., "Rough surface scattering based on the specular point theory," *IEEE Trans. Ant. and Prop.*, Vol. 16, 449–454, 1968.
32. Rémy, F., P. Shaeffer, and B. Legrésy, "Ice flow physical processes derived from ERS1 high-resolution map of Antarctica and Greenland ice sheet," *Geophys. J. Intern.*, Vol. 139, 645–656, 1999.
33. Alley, R. B. and C. R. Bentley, "Ice-core analysis on the Siple Coast of West Antarctica," *Ann. Glaciol.*, Vol. 11, 1–7, 1988.
34. Jezek, K. C. and R. B. Alley, "Effect of stratigraphy on radar-altimetry data collected over ice sheets," *Ann. Glaciol.*, Vol. 11, 60–63, 1988.
35. Goodwin, I. D., "Snow-accumulation variability from seasonal surface observations and firn-core stratigraphy, eastern Wilkes Land," *Antarctica. J. Glaciol.*, Vol. 37, No. 127, 383–387, 1991.
36. de Q. Robin, G., S. Evans, and J. T. Bailey, "Interpretation of radio echo sounding in polar ice sheets," *Phil. Trans. R. Soc.*, Vol. A265, 437–505, 1969.
37. Mätzler, C., "Applications of the interaction of microwaves with the natural snow cover," *Remote Sensing Rev.*, Vol. 2, No. 2, 259–

387, 1987.

38. Tiuri, M. E., A. E. Sihvola, E. G. Nyfors, and M. T. Hallikaiken, "The complex dielectric constant of snow at microwave frequencies," *IEEE J. Oceanic Eng.*, Vol. OE9, No. 5, 377–382, 1984.
39. Drewry, D. J. (ed.), *Antarctica: Glaciological and Geophysical Folio*, Scott Polar Research Institute, Cambridge, 1983.
40. Massonet, D., "The interferometric cartwheel: a constellation of passive satellites to produce radar images to be coherently combined," *Int. J. Remote Sensing*, Vol. 22, No. 12, 2413–2430, 2001.
41. Caparrini, M., "Using reflected GNSS signals to estimate surface features over wide ocean areas," ESTEC Working Paper 2003, December 1998.
42. Kerr, Y. H., J. Font, P. Waldteufel, and M. Berger, "The soil moisture and ocean salinity mission — SMOS," *Earth Observation Quarterly*, Vol. 66, 18–25, 2000.
43. Hamazaki, T., "Overview of the advanced land observing satellite (ALOS)," *Proc. Joint Workshop of ISPRS WG I/1, I/3 and IV/4 "Sensors and Mapping from Space 1999"*, Hannover, Germany, Sept. 27–30, 1999.